The Journal of Chemical Physics

RESEARCH ARTICLE | AUGUST 27 2025

Analyzing energy transfer with density-functional theory in real time: Time scales for the energy transfer between B850 bacteriochlorophylls

I. Schelter ; J. M. Foerster ; R. Richter ; N. Schild ; S. Kümmel

Check for updates

J. Chem. Phys. 163, 084116 (2025)
https://doi.org/10.1063/5.0279181

View Online
Export Citation

Articles You May Be Interested In

Ultrafast energy transfer between self-assembled fluorophore and photosynthetic light-harvesting complex 2 (LH2) in lipid bilayer

J. Chem. Phys. (March 2022)

Assessing density functional theory in real-time and real-space as a tool for studying bacteriochlorophylls and the light-harvesting complex 2

J. Chem. Phys. (October 2019)

Theoretical prediction of spectral and optical properties of bacteriochlorophylls in thermally disordered LH2 antenna complexes

J. Chem. Phys. (July 2006)

07 May 2026 10:57:55

AIP Advances
Why Publish With Us?
21DAYS average time to 1st decision
OVER 4 MILLION views in the last year
INCLUSIVE scope
Learn More
AIP Publishing

AIP Publishing

The Journal of Chemical Physics ARTICLE pubs.aip.org/aip/jcp

Analyzing energy transfer with density-functional theory in real time: Time scales for the energy transfer between B850 bacteriochlorophylls

Cite as: J. Chem. Phys. 163, 084116 (2025); doi: 10.1063/5.0279181
Submitted: 6 May 2025 • Accepted: 31 July 2025 •
Published Online: 27 August 2025

View Online Export Citation CrossMark

I. Schelter,[a] J. M. Foerster, R. Richter, N. Schild, and S. Kümmel

AFFILIATIONS

Theoretical Physics IV, University of Bayreuth, Bayreuth, Germany

[a]Author to whom correspondence should be addressed: ingo.schelter@uni-bayreuth.de

ABSTRACT

We present techniques that allow for predicting energy transfer in multichromophoric systems based on density-functional-theory calculations in real-time. Our work respects that the time-dependent density is the basic quantity in density-functional theory. In the approach that we discuss here, the simulations are done for a complete multimolecular system, i.e., do not require an *a priori* decomposition into subsystems. Yet, our analysis tools allow one to reliably extract energy-transfer times between different regions or constituents of the multimolecular system, the structure of transition densities, and the relative degree of excitation of constituents. We demonstrate our approach by analyzing the excitation-energy transfer between six bacteriochlorophyll molecules from the B850 ring of the light-harvesting complex 2 of the purple bacterium Rhodoblastus acidophilus. Our analysis shows that energy is transferred through this system on a time scale of ~45 fs. The spectral analysis reveals that mainly two supermolecular excitations drive the energy transfer in this system.

© 2025 Author(s). All article content, except where otherwise noted, is licensed under a Creative Commons Attribution (CC BY) license (https://creativecommons.org/licenses/by/4.0/). https://doi.org/10.1063/5.0279181

07 May 2026 10:57:55

I. INTRODUCTION

The real-time-propagation approach to time-dependent density-functional theory (TDDFT)[1–8] is excellently suited for calculating excitations of large electronic systems. It benefits from the good ratio of accuracy to computational cost that generally distinguishes density-functional-theory approaches,[9] and it scales favorably with the number of electrons.[10] A possible downside of the real-time approach is that it directly yields only the time-dependent density $n(\boldsymbol{r}, t)$. Whereas quantities such as excitation energies, oscillator strengths, and information about the nature of an excitation[11] can be obtained directly in explicitly linearized calculations such as the Casida approach,[12] all observables must be computed explicitly from $n(\boldsymbol{r}, t)$ in real-time DFT. In this paper, we demonstrate how observables and information about excitation-energy transfer can be obtained from real-time calculations, and we employ these techniques for understanding energy transfer in biological light harvesting.

Being able to understand and predict excitation-energy transfer is extremely relevant because such transfer processes play an important role in most energy-converting materials.[13–19] Paradigm examples are light-harvesting systems. Independent of whether they are biological[20–22] or manmade,[23,24] organic light-harvesting systems typically rely on transferring excitation energy between different molecular units. Being able to calculate and simulate such a process from first principles can contribute decisively to our understanding of how light harvesting can be efficient. However, for biological systems in particular, the computational challenge is huge. Such systems typically comprise many chromophores, and the latter are held in place by a protein scaffold that can itself be decisive for directing the flow of energy and charge.[25,26] Therefore, the relevant particle numbers are often in the thousands, and TDDFT remains the paradigm first-principles approach that allows for studying systems of such size.

One of the light-harvesting systems that has found particular interest in the past is the light-harvesting 2 (LH2) complex of purple bacteria,[20,27–35] schematically depicted in Fig. 1. Its electronically active part consists of two rings of bacteriochlorophyll *a* (BCL) molecules, the B800 ring and the B850 ring, which are shown in Fig. 1 surrounded by the protein scaffold. The carotenoids are not explicitly discussed in this paper. The LH2 complex acts as

© Author(s) 2025

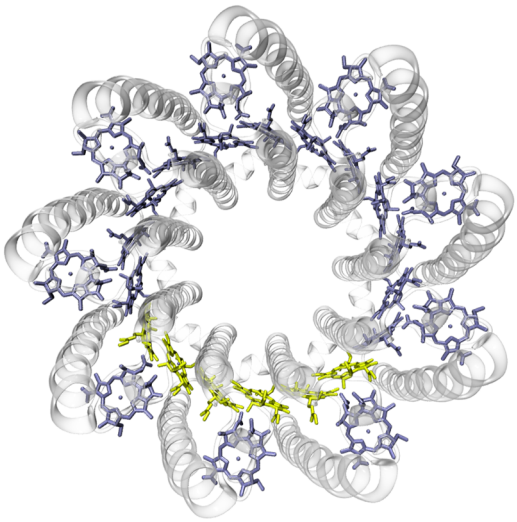

FIG. 1. Schematic illustration of the LH2 complex of Rhodoblastus (Rbl.) acidophilus (strain 10050) with protein scaffold (gray) and BCL chromophores. The carotenoids have not been depicted for clarity. The six B850 BCLs that are investigated here are highlighted in yellow. (Generated with VMD.[85])

an antenna that captures light and transfers the energy with outstanding quantum efficiency to neighboring complexes, which then channel the energy to the reaction center. Understanding the reasons for and the nature of this efficiency has been a long-standing challenge, and the question has been raised, e.g., whether quantum coherence plays a role in this context.[36–47] In the past, valuable insight has been gained in different ways, e.g., by using model Hamiltonians or via simulations that split the system of interest into subunits, such as individual molecules, and then describe the physics, such as energy transfer, by taking into account specific couplings.[18,21,44,47–70] On the one hand, such models can be studied with low computational cost and can be extended step by step to better describe and, ultimately, understand a system's properties. On the other hand, one is restricted to the respective model's limitations and underlying assumptions, e.g., the validity of a system's decomposition into its building blocks. In particular, in the B850 ring, the chromophores are very tightly packed. Therefore, instead of considering the B850 ring as 18 separate molecules with some couplings, it is more natural and adequate to treat the whole B850 ring as one large system. This type of description, which complements the existing models, is what we are aiming for with the techniques that we present in this paper.

Our approach is based on treating the multimolecular system of interest as one complete quantum mechanical system without introducing any *a priori* division into subsystems. The effects of electronic coupling and quantum mechanical coherence within the multimolecular system are thus intrinsically fully included in the calculation. We balance the computational effort by combining the real-time propagation with a representation on a real-space grid that covers a volume constructed from the union of atom-centered spheres (cf. Sec. S1 of the supplementary material for radii). This allows for a very efficient parallelization of the calculations over both the set of orbitals and the space grid, thus enabling routine calculations for thousands of electrons. From the calculation, we obtain the time-dependent density (or spin densities) of the entire system. With the techniques that we present in this work, we can extract information about the electronic excitations of the whole system, e.g., excitation energies and strengths, just from the time-dependent density. However, one can also extract information about certain parts of the system: One can, e.g., analyze which part of a system is excited at which point in time and, thus, track how excitation energy is being transferred through the system. We demonstrate this for a part of the B850 ring of the LH2 complex of Fig. 1. The nuclear coordinates are held fixed in the present simulations, and we discuss the justification for this approximation in the course of our paper.

Our paper builds on several earlier works. Reference 71 introduced the real-time real-space code BTDFT that we use here, and it also introduced the idea of accurately obtaining excitation energies and oscillator strengths from the time-dependent density by fitting the calculated dipole signal to its analytically derived form. This analysis was restricted to one specific form of excitation, the so-called boost.[72] In the present work, we extend this technique to more general excitations, we show how to analyze signals in different regions of space, and we combine our analysis with the evaluation technique of Ref. 73 for increased efficiency. Although other super-resolution techniques exist,[73–77] our method excels at disentangling clustered, spectrally close-lying excitations and their transition densities without further approximations or assumptions. Regarding the energy-transfer model, Refs. 78 and 79 developed and validated the theoretical setup for the LH2 complex that we use here for studying excitation-energy transfer between six BCLs from the B850 ring. In the energy-transfer calculations of the present work, we rely on the density-based measures of excitation energy and the molecule-specific real-space subgrids that were introduced in Ref. 80. Based on these measures, we derive further quantities that are useful for analyzing the electronic excitations in supermolecular systems, e.g., a measure for the occupation of a molecule's excited state.

Our paper is outlined as follows: We review the equations of TDDFT and some established techniques for evaluating real-time simulations in Sec. II. Section III introduces our new techniques for extracting detailed information about electronic excitations from the time-dependent density. These are then used in Sec. IV to analyze excitation-energy transfer between six bacteriochlorophylls from the B850 ring. We demonstrate how the excitation energy spreads in space and time through the system after an initial excitation, and we find that after about 45 fs, the energy has wandered through the entire system. Our article closes with a summary and conclusions in Sec. V. In the supplementary material, we present technical details (Sec. S1) and extensive derivations of the presented equations (Sec. S2). We also explain the Python[81–83] evaluation script *BTevalSpec.py* (Sec. S3) that is a valuable tool in the analysis of real-time simulations and is now available on GitHub.[84] Finally, we show additional details of the presented calculations (Sec. S4).

II. OVERVIEW: REAL-TIME DENSITY FUNCTIONAL THEORY AND ESTABLISHED EVALUATION TECHNIQUES

A. Review of basic real-time DFT equations

In real-time Kohn–Sham (KS) TDDFT, the electronic excitation of a system is described by the time-dependent electron density,

07 May 2026 10:57:55

© Author(s) 2025

$$n(\boldsymbol{r},t) = \sum_{\sigma=\uparrow,\downarrow} \sum_{j=1}^{N_\sigma} |\varphi_{j\sigma}(\boldsymbol{r},t)|^2, \tag{1}$$

where N_σ denotes the number of electrons with spin σ. The time-dependent KS orbitals $\varphi_{j\sigma}$ are the solutions of the time-dependent KS equations,

$$i\hbar\frac{\partial}{\partial t}\varphi_{j\sigma} = \underbrace{\left(-\frac{\hbar^2}{2m}\nabla^2 + v_{\text{ext}} + v_{\text{Hxc},\sigma}[n]\right)}_{h_{\text{KS},\sigma}[n]}\varphi_{j\sigma}, \tag{2}$$

where we omitted the space and time arguments for clarity of the notation. $h_{\text{KS},\sigma}$ constitutes the effective single-particle Hamiltonian of (TD)KS theory. v_{ext} is the external potential, which in our work consists of three parts. The first part is the potential generated by the atomic cores in the system, i.e., we describe the valence electrons explicitly, whereas core electrons and nuclei together are described by pseudopotentials[86,87] (cf. Sec. S1 of the supplementary material for technical details). The second part is the electrostatic potential by which we approximately take into account the chromophores' protein environment, as detailed in previous work.[78] The third part is the time-dependent potential that models the excitation. As usual,[73,76,88] light is described as a classical electric field in the dipole approximation. v_{Hxc} denotes the sum of the Hartree and exchange–correlation (xc) potential of (TD)KS theory.

The xc contribution must be approximated in practical calculations and has a strong influence on both the accuracy and the computational expense. When charge-transfer excitations are of interest, one must generally use an xc approximation that can describe these reliably, e.g., an optimally tuned range-separated hybrid.[89] These functionals have been demonstrated to describe the charge-transfer excitations that play a role in the bacterial reaction center with useful accuracy.[25,90–93] They come, however, with a substantial computational cost. In the present study, we can use the less sophisticated yet more efficient time-dependent (adiabatic) local-density approximation (TDLDA) for three reasons. First, we are predominantly interested in excitation-energy transfer, i.e., an observable that is less sensitive to shortcomings of the xc approximation than charge transfer. Second, an important aim of the present paper is to introduce methods that allow for the extraction of detailed information from real-time simulations. For introducing the methods, it is not decisive which xc approximation is used. We here use TDLDA as a convenient choice, but the introduced methods are independent of the xc approximation. That is, in future work, they can be combined with other, more advanced xc functionals. Third and finally, we have demonstrated in detail in earlier work[78,79] that in the description of the chromophores of the B850 ring, which we study here, the electrostatic potential of the protein environment shifts the spurious charge-transfer excitation energies away from the energetic range that is most relevant for the excitation-energy transfer in the B850 system. Therefore, qualitatively reliable results can be expected based on the TDLDA for the special system we study here.

The real-time approach that we use to solve the whole set of TDKS equations propagates the orbitals from Eq. (2) hand-in-hand with the time-dependent density from Eq. (1) and the TDKS potential $(v_{\text{ext}} + v_{\text{Hxc}}[n])$ on an equidistant real-space grid with grid spacing Δx using small time steps Δt. The initial state for the solution of Eq. (2) is the ground state of the system described by the ground-state (GS) density n^{GS} and the KS orbitals $\varphi_{j\sigma}^{\text{GS}}$.

This real-space and real-time approach has been used in the context of biological systems and light-harvesting questions,[75,76,78,79,88,94,95] but most of the first-principles work in this field relies on the explicitly linearized Casida equations,[12] which decompose an electronic excitation into a superposition of particle–hole transitions. However, real-time (and real-space) propagation has important advantages. The first is that it requires only the set of N occupied orbitals, but no virtual ones. For large systems, this can lead to a significant gain in computational efficiency. The real-space grid has the additional advantage that computational steps are reduced to operations involving sparse linear systems. This allows for efficient parallelization and, therefore, good parallel scaling behavior with increasing system size. Finally, a real-space grid weights the whole simulation space equally and allows one to systematically converge the grid spacing until the desired accuracy is reached. These properties make grid-based real-time TDDFT an ideal and flexible tool for studying large electronic systems.

B. Review of established techniques for calculating observables in real-time DFT

Strictly speaking, the only physical quantity that real-time DFT directly yields is the time-dependent density. Therefore, special evaluation methods are required to extract further desired physical information. In this subsection, we first review some established techniques for calculating observables from the time-dependent density before discussing new approaches in Sec. III.

The first response observable of general interest is the dipole spectrum or absorption cross section. To compute it, one traditionally[1,10,72,96] applies a so-called boost to the system's ground-state (GS) orbitals,

$$\varphi_{j\sigma}(\boldsymbol{r}, t=0) = e^{i\boldsymbol{k}\cdot\boldsymbol{r}}\varphi_{j\sigma}^{\text{GS}}(\boldsymbol{r}). \tag{3}$$

The boost is an instantaneous, spectrally broad perturbation. In essence, it corresponds to an instantaneous transfer of momentum to the orbitals. In the limit of a weak excitation, it mimics a delta-shaped electric field pulse (cf. Sec. III B). The boost vector $\boldsymbol{k}$ describes its strength and direction. After the boost, the orbitals are propagated without a further time-dependent external potential. For $t > 0$, the induced electron-density fluctuation $\delta n = n - n^{\text{GS}}$ and the induced dipole moment,

$$\delta\boldsymbol{\mu}(t) = -e\int \boldsymbol{r}\,\delta n(\boldsymbol{r},t)\mathrm{d}^3 r, \tag{4}$$

oscillate with the system's excitation frequencies ω_j in the form

$$\delta\boldsymbol{\mu}(t) = 2\sum_{j=1}^{\infty} \underbrace{A_j\boldsymbol{\mu}_j}_{=\boldsymbol{a}_j} \sin(\omega_j t) W_0^T(t), \tag{5}$$

cf. Sec. 3.1 of Ref. 71. W_0^T denotes a window function that models the finite free propagation time. Its value is 1 within $0 \le t \le T$ and 0 otherwise. Equation (5) shows that each excitation contributes to the signal with a vector amplitude $\boldsymbol{a}_j$ that is the product of the transition

07 May 2026 10:57:55

© Author(s) 2025

dipole $\boldsymbol{\mu}_j = -e\langle j|\hat{\boldsymbol{r}}|0\rangle$ from the ground state $|0\rangle$ to the excited state $|j\rangle$ and the scalar amplitude

$$A_j = -\frac{1}{e}\boldsymbol{k}\cdot\boldsymbol{\mu}_j \quad \text{(boost)}, \tag{6}$$

where e is the elementary charge and $\boldsymbol{\mu}_j$ is determined only up to a minus sign [$\delta\boldsymbol{\mu}$ in Eq. (5) is invariant under this transformation]. In general, A_j measures the strength with which an excitation is excited by the external perturbation. If one chooses the direction of the transition dipole moment so that $A_j \geq 0$, one can identify $A_j = |\langle j|\psi(t=0)\rangle| = |c_j|$ with c_j from Eq. (15) in Ref. 71, where $|\psi(t=0)\rangle$ is the wave function after the perturbation. Through the latter restriction of the transition-dipole direction, the general formalism presented in Sec. S2 of the supplementary material becomes more transparent.

The analytical form of Eq. (5) allows one to extract excitation energies and transition dipoles (or oscillator strengths) from a spectral analysis of the numerically evaluated dipole moment [Eq. (4)]. The imaginary part of the Fourier transform (denoted by F in the following, cf. Sec. S2 A of the supplementary material) of Eq. (5) yields the absorption cross section with spectral lines at the excitation energies and heights proportional to the oscillator strengths (since $|\boldsymbol{a}_j| \propto |\boldsymbol{\mu}_j|^2 \propto f_j$),

$$\mathrm{Im}\{F[\delta\boldsymbol{\mu}](\omega)\} = \sum_{j=1}^{\infty}\boldsymbol{a}_j\left[\frac{\sin[(\omega-\omega_j)T]}{\omega-\omega_j} - \frac{\sin[(\omega+\omega_j)T]}{\omega+\omega_j}\right]. \tag{7}$$

If we neglect the $\omega+\omega_j$ contributions in the latter equation, which produce spectral lines at $\omega<0$, Eq. (7) essentially corresponds to Eq. (23) from Ref. 71 with the following differences: (i) Here, we do not take the trace, (ii) we do not introduce the oscillator strengths, and (iii) we use a different minus-sign convention for the Fourier transform for convenience (i.e., we here use $e^{-i\omega t}$ for the $t\to\omega$ transformation, whereas in Ref. 71 we use $e^{+i\omega t}$). The latter ultimately leads to a global minus sign in Eq. (7) compared to Eq. (23) from Ref. 71. The artificial sine-cardinal line shape in Eq. (7) results from the finite propagation time and leads to side peaks that make a quantitative analysis by purely visual inspection difficult unless a long propagation time is employed. To damp side peaks or even get a smooth line shape, one can multiply $\delta\boldsymbol{\mu}(t)$ with a window function such as a decaying exponential $e^{-\eta t}$ with a proper $\eta>0$. In turn, however, the latter broadens the main peaks even more. As a solution, different advanced evaluation schemes have been developed[71,73,74,77] to improve the quality of the spectra while reducing the required propagation time. In Sec. III B, we extend the methods from Ref. 71, which allow the quantitative analysis of clustered spectral peaks, revealing their excitation energies, transition dipoles, oscillator strengths, and transition densities.

A second class of observables, which is particularly interesting for investigating energy-converting materials, aims at observing energy-transfer dynamics with temporal and spatial resolution. To this end, Ref. 80 discussed in detail different measures of excitation energy. Following this work, we here use

$$\varepsilon_{\dot{n}}(\boldsymbol{r},t) = [\dot{n}(\boldsymbol{r},t)]^2, \tag{8}$$

$$\mathcal{E}_{\dot{n}}^{(l)}(t) = \int_{V^{(l)}}\varepsilon_{\dot{n}}(\boldsymbol{r},t)\mathrm{d}^3r \tag{9}$$

as measures for the electronic excitation-energy density and the excitation energy per volume, respectively. The idea behind Eq. (9) is that the energy-density measure $\varepsilon_{\dot{n}}(\boldsymbol{r},t)$ is integrated over a finite volume $V^{(l)}$, e.g., the volume associated with a particular energy-accepting molecule. If one wants to analyze excitation-energy transfer through a system, then one divides the space that the system occupies into different volumes $V^{(l)}$ that do not overlap and together cover all space, i.e.,

$$V^{(l)}\cap V^{(k)} = \emptyset \qquad \text{for} \quad l\neq k \tag{10}$$

and

$$\bigcup_l V^{(l)} = \mathcal{R}^3.$$

Thus, $\sum_l \mathcal{E}_{\dot{n}}^{(l)} = \mathcal{E}_{\dot{n}}^{(\mathcal{R}^3)}$. In this paper, we choose volumes that we can assign to the BCL molecules that build the LH ring. In this way, we can analyze how the excitation energy in the LH system is distributed over the separate molecules (details in Sec. IV A).

Since the energy measure of Eq. (8) is directly derived from the induced density fluctuation, it oscillates rapidly with the excitation frequencies.[80] However, only the emerging low-frequency beating signal contains the relevant energy-transfer information. Therefore, it is helpful to smooth the signals using a Fourier filter.[80] We denote the filtered observables as $\bar{\varepsilon}_{\dot{n}}$ and $\overline{\mathcal{E}}_{\dot{n}}^{(l)}$, respectively.

III. IMPROVED REAL-TIME EVALUATION TECHNIQUES

In the following, we introduce further tools for extracting information from real-time simulations. In particular, we aim at (i) extracting detailed information about how an excitation is spatially distributed within a system and (ii) covering cases in which the excitation is not a boost but a general time-dependent dipole field.

A. Evaluating the spatial distribution of excitation energy as a function of time

A situation that frequently occurs in practice is that one is interested in the excitation-energy transfer in a system that consists of many similar molecules. Examples are films of organic semiconductor molecules[97] or the antenna complexes built from BCL molecules, as we study them in the present work. When the considered system consists of M molecules that are reasonably similar to each other and that define the molecular volumes $V^{(l)}$, $\overline{\mathcal{E}}_{\dot{n}}^{(l)}$ can be interpreted as a time-resolved molecular excitation energy.[80] In this case, one can approximate the probability of finding the system in a state in which molecule l is excited by

$$p_l(t) = \frac{\overline{\mathcal{E}}_{\dot{n}}^{(l)}(t)}{\sum_{k=1}^{M}\overline{\mathcal{E}}_{\dot{n}}^{(k)}(t)}. \tag{11}$$

The latter allows one to evaluate an inverse participation ratio[11,98] (IPR) as a measure for the time-dependent delocalization of the excitation energy over molecular units via the definition

$$\mathrm{IPR}(t) = \frac{1}{\sum_{l=1}^{M}[p_l(t)]^2}. \tag{12}$$

07 May 2026 10:57:55

© Author(s) 2025

In the limiting cases of full localization ($p_l = 1$ for one specific l and 0 otherwise), the IPR assumes 1. In the case of full delocalization ($p_l = 1/M$ for all l), the IPR assumes M. From a real-time simulation perspective, this is an easy-to-evaluate measure with a straightforward interpretation that does not require a spectral analysis.

B. Evaluating dipole signals as a function of frequency

We now look at situations where the excitation is not a boost but a weak perturbation with a scalar potential $V(\boldsymbol{r})h(t)$ that acts in a finite time interval $-T_e \le t \le 0$ on the ground state with a multiplicative $V \in \mathcal{R}$ and time profile $h \in \mathcal{R}$. Furthermore, we assume that the system of interest is built from several molecules. Then, one can record the dipole moment in each of the molecular volumes $V^{(l)}$, and one can write the equivalents of Eqs. (4) and (5) for each $V^{(l)}$,

$$\delta\boldsymbol{\mu}^{(l)}(t) = -e\int_{V^{(l)}} \mathbf{r}\,\delta n(\mathbf{r},t)\mathrm{d}^3 r \tag{13}$$

and

$$\delta\boldsymbol{\mu}^{(l)}(t) = 2\sum_{j=1}^{\infty} \underbrace{A_j\boldsymbol{\mu}_j^{(l)}}_{=\boldsymbol{a}_j^{(l)}} \sin(\omega_j t + \phi_j) W_0^T(t). \tag{14}$$

The superscript (l) carries over to the amplitude vectors $\mathbf{a}_j^{(l)}$ and the transition dipoles $\boldsymbol{\mu}_j^{(l)}$, which are the molecular contributions to $\boldsymbol{a}_j$ and $\boldsymbol{\mu}_j$, i.e., $\boldsymbol{\mu}_j = \sum_l \boldsymbol{\mu}_j^{(l)}$. Compared to Eq. (5), each excitation in Eq. (14) further gains a specific phase ϕ_j, which can be determined from the argument of the spectral profile $\tilde{h} = F[h]$ of the external perturbation at the respective excitation energies,

$$\phi_j = \arg\left[\tilde{h}(\omega_j)\right]. \tag{15}$$

For a boost excitation, all phases ϕ_j equal 0, but they assume finite values when the excitation is not a boost. The scalar amplitudes A_j are the product of the modulus of the spectral profile $|\tilde{h}|$ at the excitation energies and the overlap integral between the respective transition density $n_j = \langle j|\hat{n}|0\rangle$ and the spatial profile V of the excitation,

$$A_j = \frac{1}{\hbar}\int n_j(\boldsymbol{r})V(\boldsymbol{r})\mathrm{d}^3 r\,|\tilde{h}(\omega_j)|. \tag{16}$$

In the case of an electric field in dipole approximation with $V = V^{\mathrm{E}} \equiv -e\boldsymbol{E}\cdot\boldsymbol{r}$ and constant $\boldsymbol{E}$, the amplitudes reduce to

$$A_j = -\frac{1}{\hbar}\boldsymbol{E}\cdot\boldsymbol{\mu}_j\,|\tilde{h}(\omega_j)| \quad (\mathrm{E-field}). \tag{17}$$

The derivation of the above equations for this general case is long and fraught with detail. Therefore, we here focus on the results and report the detailed derivation in Sec. S2 of the supplementary material. [There, we also discuss perturbations that are of a more general form than the separable product $V(\boldsymbol{r})h(t)$ that we look at here]. We note in passing that the known result for the case of a boost excitation, Eq. (6), results from Eq. (17) for the potential $Vh(t) = V^{\mathrm{boost}}h(t) \equiv -\hbar\boldsymbol{k}\cdot\boldsymbol{r}\delta(t)$, i.e., we thus showed that the boost excitation can be written as a time-dependent potential.

Computing the Fourier transform of Eq. (14) leads to

$$F[\delta\boldsymbol{\mu}^{(l)}](\omega) = \sum_{j=1}^{\infty} A_j\boldsymbol{\mu}_j^{(l)}\left[e^{-i\phi_j}L_0^T(\omega+\omega_j) - e^{+i\phi_j}L_0^T(\omega-\omega_j)\right], \tag{18}$$

where the line shape function L_0^T is given by

$$L_0^T(\omega) = iF\left[W_0^T\right] = \frac{1-\cos(\omega T)}{\omega} + i\frac{\sin(\omega T)}{\omega}. \tag{19}$$

For a boost, the imaginary part of Eq. (18) reduces to Eq. (7).

Inserting Eq. (17) into Eq. (18) yields the key equation that allows us to accurately obtain energies and transition dipoles via a fit to $F[\delta\boldsymbol{\mu}^{(l)}]$. The simulation and evaluation procedure for how to do this is the following: After computing the system's ground state, one starts to propagate under the influence of an excitation such as an electric field with a given amplitude, frequency, and time profile with duration T_e. In the subsequent free propagation $0 \le t \le T$, one records $\delta\boldsymbol{\mu}^{(l)}$ according to Eq. (13) in M volumes $V^{(l)}$ that are, e.g., associated with the different molecules. From the Fourier transform of the latter, one gains $6M$ scalar spectra from (i) M spatial regions, (ii) three spatial vector components (x, y, z), as well as (iii) real and imaginary parts (factor 2). To these spectra, we simultaneously fit $(1 + 3M)$ parameters for each excitation: one energy ω_j and $3M$ components of $\boldsymbol{\mu}_j^{(l)}$ or $\mathbf{a}_j^{(l)}$, respectively. The fit is done by increasing the number of excitations [index j in Eq. (14)] one by one or in small batches. Error and significance measures are used to ensure the quality of the fit (cf. Secs. S3 C and S3 F of the supplementary material). Despite the large number of fit parameters, this whole procedure leads to very good results also for closely lying excitations since the fit parameters must be consistent over all spectra. We developed scripts that allow the fit to be done semi-automatically with minimal manual adjustment; cf. Sec. S3 H of the supplementary material for examples.

Of course, excitations that are not excited by the initial perturbation (e.g., if their transition dipole is orthogonal to the field polarization) cannot be seen and require a further, complementary simulation with a different external-field polarization. Excitations with zero oscillator strength, on the other hand, can be made visible with a perturbation that breaks dipole symmetry, e.g., one that is spatially localized.

After fitting the excitation spectrum, one can also obtain the transition densities by generalizing the procedure described in Ref. 71. In essence, one can write the analogs of Eqs. (14) and (18) for the whole density by replacing the induced dipole moment by the induced density and the transition dipoles by the transition densities n_j,

$$\delta n(\boldsymbol{r},t) = 2\sum_{j=1}^{N_{\mathrm{ex}}} A_j n_j(\boldsymbol{r})\sin(\omega_j t + \phi_j)W_0^T(t), \tag{20}$$

$$F[\delta n](\boldsymbol{r},\omega) = \sum_{j=1}^{N_{\mathrm{ex}}} \boldsymbol{A}_j n_j(\boldsymbol{r})\left[e^{-i\phi_j}L_0^T(\omega+\omega_j) - e^{+i\phi_j}L_0^T(\omega-\omega_j)\right]. \tag{21}$$

07 May 2026 10:57:55

© Author(s) 2025

After the fit to the spectrum, the number of excitations N_{ex} and the values of ω_j, A_j, and ϕ_j are known. After evaluating the Fourier-transformed density at the excitation energies $F[\delta n](\boldsymbol{r}, \omega_j)$ for $j = 1, \ldots, N_{ex}$ (which can be complex valued for a general external excitation), one can use Eq. (21) to disentangle the set of $F[\delta n](\boldsymbol{r}, \omega_j)$ and retrieve the proper (real-valued) transition densities n_j without further fitting. The derivation of the equations is reported in Sec. S2 C of the supplementary material, together with a description of the script *BTevalSpec.py* in Sec. S3 that we use for the evaluation of the fits. This script is now publicly available on GitHub. An example is given in Sec. S3 H of the supplementary material.

IV. B850 ENERGY TRANSFER FROM A REAL-TIME PERSPECTIVE

We now use the techniques described above to analyze excitation energy transfer within a part of the B850 ring of the LH2 complex of Rbl. acidophilus (strain 10050).[27,28]

A. Setup and simulation parameters

For these simulations, we used the crystal structure that we first used in Ref. 78 and which was determined by Cogdell *et al.*[99] at a resolution of 1.85 Å. The naming scheme and orientation in the coordinate system follow the 1NKZ[100] structure, which shows one third of the complete ring. The ring consists of three repeat units with six BCLs each. The latter are called B301 to B306. After completing the ring by 120° and 240° rotations around the z-axis, we get three symmetry representations, which we denote by the suffix "a" (original), "b" (120°), or "c" (240°). In the present work, we consider the BCLs B306c and B301a–B305a. For brevity of notation, they are called B1–B6 in the following. B1–B6 make up one third of the B850 ring, as highlighted in Fig. 1 and shown in the top panel of Fig. 2. These BCLs build three α/β dimers, of which B1, B3, and B5 are β and B2, B4, and B6 are α BCLs.

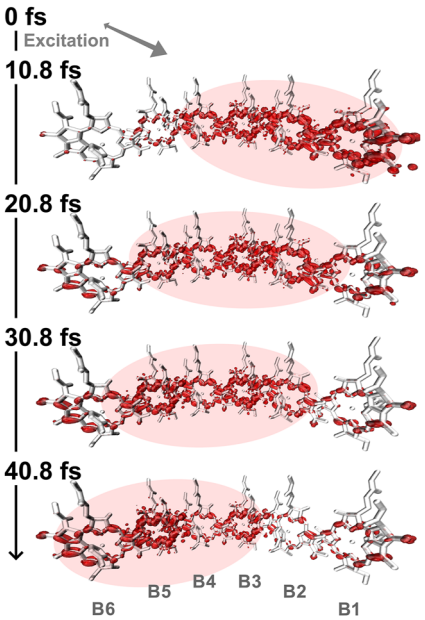

FIG. 2. Snapshots of $\bar{\varepsilon}_n$ (iso value 0.04 a.u.) at four different times after the excitation. The ellipses indicate the regions of high excitation-energy content. One can see that the excitation energy spreads from right to left. See the main text for details. (Partly generated with VMD.[85])

The BCLs B2–B4, i.e., B301a–B303a, were already used in earlier work, and we prepared the system in analogy to Sec. II A of Ref. 78. We truncated the phytyl tails of the BCLs and replaced them with a methyl group each, and we explicitly took into account the histidine residues that coordinate the central Mg atoms of the six BCLs. We cut these histidine residues off from the protein backbone between the respective C_α and C_β and saturated them each with an H-atom. Earlier work showed[78] that one can describe the BCLs' Q-band excitations reasonably well by including the histidine residues explicitly while describing the rest of the protein, the other chromophores within the LH2 complex, and the LH2's environment by an electrostatic potential, as detailed in Sec. II B of Ref. 78. Thus, the whole simulation system consists of the six BCLs (without phytyl tails), their coordinating histidine residues, and the electrostatic environment potential. In the following, unless stated otherwise, we treat one BCL and its coordinating histidine residue as a unit.

We excite the system by applying an electric dipole field that extends through the entire simulation domain,

$$V^E(\boldsymbol{r}, t) = -e\underbrace{\sqrt{\frac{2I}{c\varepsilon_0}}\,\hat{\boldsymbol{p}}}_{=\boldsymbol{E}} \cdot \boldsymbol{r}\ \underbrace{\sin\left[\omega^E(t+T_e)\right] f(t+T_e)}_{=h(t)} \tag{22}$$

with polarization $\hat{\boldsymbol{p}} = (2, -1, 0)/\sqrt{5}$, light intensity $I = 10^7$ W/cm^2, and energy $\hbar\omega^E = 0.1270$ Ry ≈ 1.728 eV. The envelope

$$f(t) = \begin{cases} t/T_r, & t \in [0; T_r[, \\ 1, & t \in [T_r; T_e - T_r[, \\ 1 - [t - (T_e - T_r)]/T_r, & t \in [T_e - T_r; T_e], \\ 0, & \text{else} \end{cases} \tag{23}$$

describes a pulse shape with a total duration of $T_e = 10$ fs composed of a $T_r = 1$ fs ascending ramp followed by a $T_e - 2T_r = 8$ fs plateau and a final $T_r = 1$ fs descending ramp. Thus, the field simulates a weak incident laser pulse with linear polarization. Its excitation energy is close to the Q_y excitation energies that we found[78] for the single BCLs at this level of theory, and the spectral width of the pulse covers the whole range of coupled Q_y excitations of the complex. We chose the polarization such that B1 and B2 are excited the strongest, and B5 and B6 only weakly, by approximately matching the polarization to the transition dipole of B1 and B2. The arrow at the top of Fig. 2 indicates the polarization vector. The spectral profile of the excitation is shown in Fig. 11 of the supplementary material.

For analyzing the results, we split up the whole simulation space into six volumes, one for each BCL-histidine residue unit. The volumes are labeled by a superscript (l), and observables are recorded in these volumes as explained in Sec. III A. For our purposes, it was sufficient to define the volumes in the following way: For each grid point, we determined the atom closest to it. We then assigned that grid point to the molecular area to which the atom belongs. However, if required, one can also use more elaborate methods[75,101] to

07 May 2026 10:57:55

© Author(s) 2025

define a decomposition. Further numerical details are given in Sec. S1 of the supplementary material, along with additional technical information about the evaluation.

B. Excitation energy transfer analyzed in real time

Figures 2–4 visualize the first set of central results. They show how excitation energy spreads through the system as a function of time. The excitation starts at 0 fs, i.e., the external field acts from 0 to 10 fs. The panels of Fig. 2 show snapshots of $\bar{\varepsilon}_{\hat{n}}$, i.e., a measure for the excitation-energy density, between about 10 and 40 fs, i.e., shortly after the external perturbation ended. Figure 2 is complemented by Fig. 3, which shows the evolution of the excitation energies of BCL dimers as measured by $\overline{\mathcal{E}}_{\hat{n}}^{(l)}$, but here evaluated not for one unit's volume, but for a pair of BCLs. The arrows in Fig. 3 mark the positions at which the snapshots of Fig. 2 have been taken.

During the excitation period, the excitation energy increases steeply on B1–B4 (Fig. 3). B1 and B2 are the most excited since their Q_y transition dipoles best match the polarization of the external field. The top snapshot of Fig. 2 shows the situation directly after the external perturbation has ended. Thereafter, the excitation energy spreads rapidly over B3 and B4 (≈15–32 fs) toward B5 and B6 (>32 fs) on a 40–50 fs time scale. The latter time interval expresses the uncertainty, especially in defining the starting time for the spreading of the energy, which can already start at the beginning of the initial excitation period. Thus, the upper bound is likely the more accurate and relevant value.

The IPR curve in Fig. 4 shows a delocalization that initially varies between 4 and 5 BCL units during the first 30 fs, followed by a localization toward 2 BCL units for later times. The initial variations, especially during the excitation period, should not be overinterpreted due to the approximate character of the probabilities defined in Eq. (11). The IPR, thus, suggests a delocalization over about 4.5 BCL units during the first 30 fs, which is in line with Figs. 2 and 3. The following localization can be explained by the finite extent of the simulation system that we truncated beyond B6. Figures 2 and 3 both show that the energy starts localizing on B5/B6 for $t > 30$ fs,

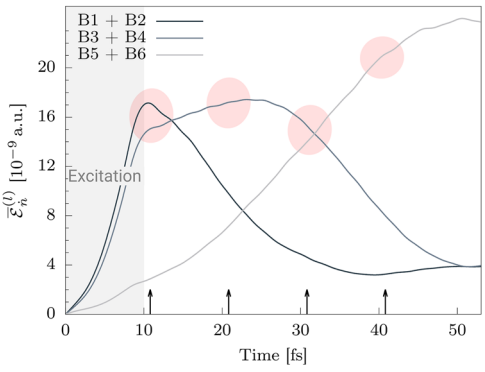

FIG. 3. Each line depicts $\overline{\mathcal{E}}_{\hat{n}}^{(l)}$ for a pair of BCLs as indicated in the upper left corner. One can see excitation energy transfer from B1/B2 over B3/B4 to B5/B6. Arrows on the time axis correspond to the snapshots in Fig. 2. The ellipses highlight the largest contributions of BCL pairs to the excitation energy at those time stamps and connect to the ellipses in Fig. 2. The external perturbation is active for the first 10 fs.

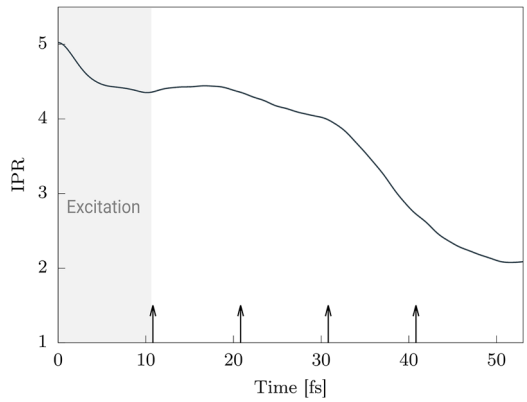

FIG. 4. Evolution of the excitation's IPR as a measure for the excitation's delocalization over BCL units. Arrows on the time axis correspond to the snapshots in Fig. 2.

which explains the decreasing IPR. For even longer propagation times, this truncation even leads to a backward reflection of the excitation energy. This artificial dynamics is, however, not shown in our figures.

On the time scale of ~50 fs that we study here, the frozen nuclei approximation is expected to be very well justified due to the relatively low velocity. Therefore, it is not expected that, e.g., nuclear movement would break the electronic coherence on this short time scale. However, future work that aims to study the full B850 ring and longer time scales will need to take the nuclear motion into account.

C. Excitation energy transfer analyzed in frequency space

The real-time evaluation of energy-transfer signals is very intuitive. However, a complementary analysis in frequency space can also be instructive, as it can reveal information about the aggregate's electronic excitations that drive the observed energy transfer, as well as the molecular contributions to these excitations. To this end, we recorded the single BCLs' contributions to the induced dipole moment by integrating over the respective volumes $l = 1, \ldots, 6$, cf. Eq. (13). From these, we obtained spectra and, ultimately, precise values for excitation energies, strengths, and transition dipoles as described in Sec. III B and as further detailed in Sec. S4 of the supplementary material. We summarize the resulting values for energies $\hbar\omega_j$, phases ϕ_j, and amplitude vectors $\mathbf{a}_j^{(l)}$ in Table I (Sec. S4) of the supplementary material.

Our evaluation reveals five excitations in the energy range from 1.6 to 1.8 eV, in which one expects the coupled Q_y excitations. We label the latter by σ_j with $j \in 1, 2, 3, 4, 5$ in ascending energetic order. The spectrum is shown on the left-hand side of Fig. 5, i.e., on the vertical axis from top to bottom. Red lines mark the excitation energies. The continuous black curves result from broadening the spectrum with a Gaussian with a width of 0.005 eV as a guide to the eye. Each of the six BCLs contributes to each of the five excitations with its own dipole response. The strength of each contribution is given by the molecular amplitude vectors $\boldsymbol{a}_j^{(l)}$.

07 May 2026 10:57:55

© Author(s) 2025

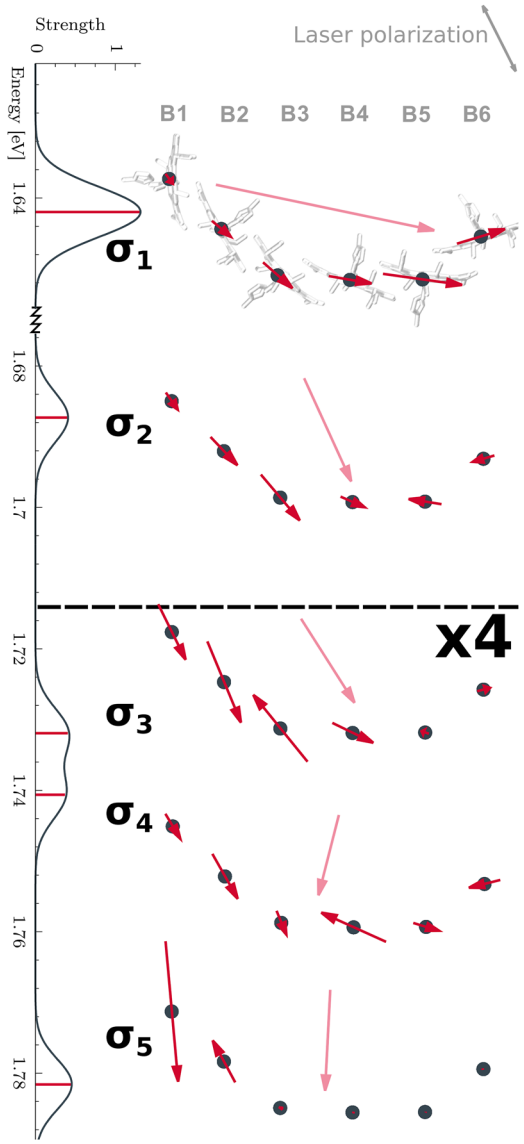

FIG. 5. Vertical axis: Excitation spectrum of the 6 BCL system. One can see five excitations $\sigma_j, j = 1, \ldots, 5$, with energy increasing from top to bottom, and with the peak heights reflecting the oscillator strengths f_j. To the right of each excitation, the structure of the BCL system is indicated by black dots marking the positions of the BCL molecules (the full molecular structure is indicated once to the right of σ_1). Red arrows visualize the dipole amplitude $\boldsymbol{a}_j^{(l)}$ with which this BCL contributes to the given excitation. Pale red arrows visualize the total dipole amplitude, $\boldsymbol{a}_j$, for the given excitation. Oscillator strengths and vectors of the excitations below the vertical dashed black line, i.e., σ_3–σ_5, are scaled up by a factor of 4.

Figure 5 visualizes the contribution of each BCL molecule to each excitation in the following way: The molecular structure of the BCL system is shown to the right of σ_1, i.e., at the top of the figure. For the other excitations, only the central Mg atom of each BCL is shown to the right of the excitation's position on the energy axis for clarity of the visual impression. The saturated red arrows show the projection of the molecular dipole amplitude $\boldsymbol{a}_j^{(l)}$ onto the xy plane for each BCL. The total dipole amplitude vectors $\boldsymbol{a}_j = \sum_{l=1}^{6} \boldsymbol{a}_j^{(l)}$ are shown as pale red arrows. The latter are parallel to the respective excitation's transition dipole since $\boldsymbol{a}_j \propto \boldsymbol{\mu}_j$; cf. Eq. (14). For better visualization of the excitations with low oscillator strengths, i.e., σ_3 to σ_5, we scaled their oscillator strengths and arrow lengths up by a factor of 4. The polarization of the initial perturbation is shown in the top right corner.

The five excitations lie between 1.642 and 1.782 eV, i.e., span an energy range of about 0.14 eV. For comparison, the Q_y excitation energy of a single B850 BCL with the same level of theory lies within this range, e.g., 1.753 eV for B3 (B302a).[78] The first two excitations at 1.642 and 1.687 eV are associated with the largest response and are completely delocalized, with all BCLs contributing significantly. Visually inspecting the transition densities (shown in Sec. S4 B and Fig. 12 of the supplementary material) reveals that the supermolecular excitations can qualitatively be described as superpositions of the BCLs' Q_y excitations. As expected from an (imperfect) J-aggregate, the lowest-energy excitation σ_1 shows a constructive superposition of all BCL contributions, i.e., all BCLs are in phase. The situation is different for σ_2: The contributions of B5 and B6 to the second excitation, i.e., the amplitudes $\boldsymbol{a}_2^{(5)}$ and $\boldsymbol{a}_2^{(6)}$, are almost opposite to how B5 and B6 contribute to σ_1. For the given exciting field, i.e., for the chosen external perturbation of Eq. (23), both σ_1 and σ_2 contribute significantly to the total dipole signal. This is seen from the comparable lengths of the pale red arrows in Fig. 5. However, whereas σ_1 has the larger oscillator strength, σ_2 is excited more efficiently since its polarization and frequency better match the external perturbation. As a side remark, we note that the excitation energies of σ_1 and σ_2 are lower than that of a single B850 BCL (~1.76–1.77 eV for B2–B4[78] at the given level of theory), i.e., we see a net red shift of the absorption, as expected from an effective J-aggregate.[20]

The remaining three excitations at 1.732, 1.741, and 1.782 eV show an overall weaker response with mixed contributions mostly from B1–B4. Therefore, σ_3 to σ_5 hardly participate in the energy transfer to B5–B6. Another interesting observation is that the dipole contributions of the same BCL to different excitations are, in general, not perfectly parallel to each other (compare the arrow directions for a single BCL vertically for different excitations). A good example is B1. It contributes, among others, to excitations σ_2 and σ_5, but the respective vectors' directions are significantly different. This means that the supermolecular excitations that we see cannot be described well as simple superpositions of the Q_y excitations of the single BCLs. If the latter were the case, then the dipole contributions of a given BCL to different excitations would be parallel. To support this argument, we show and discuss the transition densities in Sec. S4 B of the supplementary material. Finally, we note that an exciton model would predict six excitations from the coupled Q_y excitations of the six BCLs. Indeed, in a simulation with orthogonal external-field polarization (shown in Sec. S4 C of the supplementary material), we find a sixth excitation at 1.725 eV. The latter qualitatively resembles σ_5 but is localized on B5 and B6 with a transition dipole that is almost orthogonal to the polarization of the external field that was used in the simulation discussed in this section. Hence, it is not excited in the simulation discussed above and, therefore, is neither visible in the spectrum nor participates in the observed energy transfer.

07 May 2026 10:57:55

© Author(s) 2025

Putting together the above observations, the following picture emerges: The energy transfer that we saw in the time domain in Sec. IV B is primarily driven by just the two excitations σ_1 and σ_2. This can be concluded for two reasons: (i) a large dipole amplitude at one site in frequency space also corresponds to a potentially large value of $\overline{\mathcal{E}}_n^{(l)}$ in time-space at the same site, and (ii) only σ_1 and σ_2 have significant contributions from B5 and B6. We thus conclude that the energy difference between σ_1 and σ_2 determines the energy-transfer time scale in the presented setup. Since both σ_1 and σ_2 are considerably excited, we see a substantial energy transfer.

To clarify the former statements, we rephrase them in a thought experiment and ignore σ_3–σ_5 for simplicity. At some point in time after the initial excitation, σ_1 and σ_2 interfere constructively on B1–B4 and destructively on B5–B6, which corresponds to an energy concentration on B1–B4. The superposition of two excitations results in a beating signal.[102] Half a beating period after the energy was concentrated on B1–B4, i.e., after $T_{1,2}^{\text{beat}}/2 = \pi/(\omega_2 - \omega_1) \approx 45$ fs, the superposition is reversed. Thus, the energy is then concentrated on B5–B6. In Fig. 3, this situation occurs at the end of the shown time interval at about 50 fs. At this point in time, B5 has reached its highest level of excitation.

Since the energy difference between σ_1 and σ_2 is only about 50 meV, small variations of this setup, e.g., due to changes in the simulation or due to environmental effects,[26,103,104] can have a significant influence on the time scale of energy transfer. Furthermore, it is clear that this type of energy transfer is reversible, as the beating signal keeps repeating. The irreversible "downhill energy transfer" that drives photosynthesis results from the interplay with the nuclear degrees of freedom, as discussed in the Conclusions.

V. CONCLUSIONS

The work that we presented in this paper has two aims. On the one hand, we presented techniques for extracting observables from real-time propagation calculations, with a particular focus on excitation-energy transfer. These techniques can be applied in combination with any quantum mechanical approach that yields the time-dependent density. We showed that combining evaluations in time space and frequency space can yield complementary insights and allows for unraveling even complicated dynamics in multichromophoric supermolecular systems.

On the other hand, we used our techniques to study excitation energy transfer in a system of six BCL molecules, B1–B6, that form a fraction of the B850 ring of the LH2 complex of purple bacteria. In these calculations, we relied on TDDFT in real-time on a real-space grid. After an initial excitation of 10 fs length that was chosen to mostly excite B1 and B2, the analysis in real-time revealed a rapid delocalization of the excitation energy within the 6-BCL system on a time scale of 40–50 fs and a delocalization over about 4.5 BCL units.

We complemented this analysis in real time with an analysis in frequency space, decomposing the dipole response into separate contributions from the six BCLs for each of the five electronic excitations that we found. The first, dominant excitations, σ_1 at 1.642 eV and σ_2 at 1.687 eV, contribute with a similar magnitude to the dipole response. The decomposition into molecular contributions reveals that σ_1 and σ_2 also predominantly drive the energy transfer from B1–B4 to B5–B6. Using the energy difference between σ_1 and σ_2, we could thus estimate the energy-transfer time scale from B1–B4 to B5–B6 to be about 45 fs, which is in good agreement with the time-space analysis.

Finally, we want to put these calculations into the broader context of excitation-energy transfer in light-harvesting systems. First, it is clear that due to the approximations that we made, e.g., with respect to the description of the exchange–correlation effects, the truncation of the system, and the approximate environment potential, our results, e.g., the obtained excitation energies, cannot be compared quantitatively to experimental numbers. However, as discussed in Sec. I, one can expect that qualitatively our simulations capture the correct physics. Second, the processes that we study here focus on the quantum mechanically coherent electronic excitation dynamics. Due to the clamped nuclei, no dissipation is present in our simulations. On the time scale of a few tens of femtoseconds that we discuss here, neglecting the nuclear motion appears justified. It is, however, obvious that with clamped nuclei, the concentration of excitation energy that we observe on B5 and B6 after about 50 fs will redistribute again at later times. Yet our simulations clearly reveal a mechanism that is a relevant first step in excitation-energy transfer: The superposition of electronic excitations leads to beating signals in analogy to the beats that one observes in coupled oscillators. The resulting constructive and destructive interference concentrates excitation energy in certain localized regions of space on the time scale that is set by the beat. When nuclear motion, or more generally speaking, the effects of an environment, change the structure of the system on a similar time scale, then the nuclear or environmental effects can break the original beating signal and lead to the localization of the excitation energy. In this sense, our simulations yield a first-principles estimate for the time scale that is relevant for the first step of excitation-energy transfer. A relevant field of future work is to go beyond the clamped nuclei approximation. This can be achieved, e.g., by coupling classical nuclear motion with propagation of the real-time Kohn–Sham equations or by taking environmental effects into account via stochastic TDDFT.[105]

SUPPLEMENTARY MATERIAL

In the supplementary material, we present numerical details for the presented simulation in Sec. S1, the theory of the spectral evaluation methods in Sec. S2, details about the implementation of the *BTevalSpec.py* script (which is available on GitHub), together with selected examples in Sec. S3, and details on the evaluation of the 6-BCL simulation in Sec. S4.

ACKNOWLEDGMENTS

We are grateful to Thomas Trepl and Jürgen Köhler for many insightful discussions. We acknowledge the support by the "Biological Physics" program of the Elite Network of Bavaria and by the Bavarian State Ministry of Science, Research, and the Arts via the Collaborative Research Network "Solar Technologies go Hybrid." We gratefully acknowledge the scientific support and HPC resources provided by the Erlangen National High Performance Computing Center (NHR@FAU) under the NHR project ELTRANS. Computer

07 May 2026 10:57:55

© Author(s) 2025

hardware was partially funded by the German Research Foundation (DFG) at NHR@FAU under Grant No. 440719683 and at the Bayreuth Center for High Performance Computing under Grant No. 422127126.

AUTHOR DECLARATIONS

Conflict of Interest

The authors have no conflicts to disclose.

Author Contributions

I.S. and S.K. conceptualized the work. I.S. worked out the theory and the equations, wrote most of the routines, supervised further code development, and ran all calculations. N.S. implemented the Chebyshev filter algorithm. I.S. and R.R. implemented the evaluation script. I.S. created all figures in discussion with S.K. and R.R. J.F. generated the protein environment potential. I.S. and S.K. wrote the paper together. All authors discussed the results and the final paper.

I. Schelter: Conceptualization (equal); Data curation (lead); Formal analysis (lead); Investigation (lead); Methodology (lead); Project administration (supporting); Software (lead); Validation (lead); Visualization (lead); Writing – original draft (equal); Writing – review & editing (equal). **J. M. Foerster**: Formal analysis (supporting); Investigation (supporting); Methodology (supporting); Validation (supporting); Visualization (supporting); Writing – review & editing (supporting). **R. Richter**: Formal analysis (supporting); Investigation (supporting); Software (supporting); Writing – review & editing (supporting). **N. Schild**: Methodology (supporting); Software (supporting). **S. Kümmel**: Conceptualization (equal); Formal analysis (supporting); Funding acquisition (lead); Investigation (supporting); Methodology (supporting); Project administration (lead); Supervision (lead); Validation (supporting); Visualization (supporting); Writing – original draft (equal); Writing – review & editing (equal).

DATA AVAILABILITY

The data that support the findings of this study are available within the article and its supplementary material, the evaluation script *BTevalSpec.py* is available on GitHub,[84] and the data that support the findings of this study are available from the corresponding author upon reasonable request.

REFERENCES

[1]F. Calvayrac, P. G. Reinhard, and E. Suraud, "Spectral signals from electronic dynamics in sodium clusters," Ann. Phys. **255**, 125–162 (1997).
[2]M. A. L. Marques and E. K. U. Gross, "Time-dependent density functional theory," Annu. Rev. Phys. Chem. **55**, 427–455 (2004).
[3]M. A. L. Marques, N. T. Maitra, F. M. S. Nogueira, E. K. U. Gross, and A. Rubio, *Fundamentals of Time-Dependent Density Functional Theory*, *Lecture Notes in Physics*, edited by M. A. L. Marques, N. T. Maitra, F. M. Nogueira, E. K. U. Gross, and A. Rubio (Springer, Berlin, Heidelberg, 2012), Vol. 837.
[4]M. R. Provorse and C. M. Isborn, "Electron dynamics with real-time time-dependent density functional theory," Int. J. Quantum Chem. **116**, 739–749 (2016).
[5]X. Li, N. Govind, C. Isborn, A. E. DePrince, and K. Lopata, "Real-time time-dependent electronic structure theory," Chem. Rev. **120**, 9951–9993 (2020).
[6]N. Tancogne-Dejean, M. J. T. Oliveira, X. Andrade, H. Appel, C. H. Borca, G. Le Breton, F. Buchholz, A. Castro, S. Corni, A. A. Correa, U. De Giovannini, A. Delgado, F. G. Eich, J. Flick, G. Gil, A. Gomez, N. Helbig, H. Hübener, R. Jestädt, J. Jornet-Somoza, A. H. Larsen, I. V. Lebedeva, M. Lüders, M. A. L. Marques, S. T. Ohlmann, S. Pipolo, M. Rampp, C. A. Rozzi, D. A. Strubbe, S. A. Sato, C. Schäfer, I. Theophilou, A. Welden, and A. Rubio, "Octopus, a computational framework for exploring light-driven phenomena and quantum dynamics in extended and finite systems," J. Chem. Phys. **152**, 124119 (2020); arXiv:1912.07921.
[7]C. Shepard, R. Zhou, D. C. Yost, Y. Yao, and Y. Kanai, "Simulating electronic excitation and dynamics with real-time propagation approach to TDDFT within plane-wave pseudopotential formulation," J. Chem. Phys. **155**, 100901 (2021).
[8]J. Hekele, Y. Yao, Y. Kanai, V. Blum, and P. Kratzer, "All-electron real-time and imaginary-time time-dependent density functional theory within a numeric atom-centered basis function framework," J. Chem. Phys. **155**, 154801 (2021).
[9]W. Kohn, "Nobel Lecture: Electronic structure of matter—Wave functions and density functionals," Rev. Mod. Phys. **71**, 1253–1266 (1999).
[10]K. Yabana and G. F. Bertsch, "Time-dependent local-density approximation in real time: Application to conjugated molecules," Int. J. Quantum Chem. **75**, 55–66 (1999).
[11]J. M. Herbert, "Visualizing and characterizing excited states from time-dependent density functional theory," Phys. Chem. Chem. Phys. **26**, 3755–3794 (2024).
[12]M. E. Casida, "Time-dependent density functional response theory for molecules," in *Recent Advances in Density Functional Methods* (World Scientific, 1995), pp. 155–192.
[13]B. Albinsson and J. Martensson, "Long-range electron and excitation energy transfer in donor–bridge–acceptor systems," J. Photochem. Photobiol., C **9**, 138–155 (2008).
[14]Y.-C. Cheng and G. R. Fleming, "Dynamics of light harvesting in photosynthesis," Annu. Rev. Phys. Chem. **60**, 241–262 (2009).
[15]F. Laquai, Y. Park, J. Kim, and T. Basché, "Excitation energy transfer in organic materials: From fundamentals to optoelectronic devices," Macromol. Rapid Commun. **30**, 1203–1231 (2009).
[16]T. Renger, "Theory of excitation energy transfer: From structure to function," Photosynth. Res. **102**, 471–485 (2009).
[17]L. Cupellini, M. Corbella, B. Mennucci, and C. Curutchet, "Electronic energy transfer in biomacromolecules," Wiley Interdiscip. Rev.:Comput. Mol. Sci. **9**, e1392 (2019).
[18]S. Kundu and N. Makri, "Intramolecular vibrations in excitation energy transfer: Insights from real-time path integral calculations," Annu. Rev. Phys. Chem. **73**, 349–375 (2022).
[19]D. Zigmantas, T. Polívka, P. Persson, and V. Sundström, "Ultrafast laser spectroscopy uncovers mechanisms of light energy conversion in photosynthesis and sustainable energy materials," Chem. Phys. Rev. **3**, 041303 (2022).
[20]R. J. Cogdell, A. Gall, and J. Köhler, "The architecture and function of the light-harvesting apparatus of purple bacteria: From single molecules to *in vivo* membranes," Q. Rev. Biophys. **39**, 227–324 (2006).
[21]C. Curutchet and B. Mennucci, "Quantum chemical studies of light harvesting," Chem. Rev. **117**, 294–343 (2017).
[22]S. J. Jang and B. Mennucci, "Delocalized excitons in natural light-harvesting complexes," Rev. Mod. Phys. **90**, 035003 (2018).
[23]J.-L. Brédas, J. E. Norton, J. Cornil, and V. Coropceanu, "Molecular understanding of organic solar cells: The challenges," Acc. Chem. Res. **42**, 1691–1699 (2009).
[24]M. Jacobs, J. Krumland, and C. Cocchi, "Laser-controlled charge transfer in a two-dimensional organic/inorganic optical coherent nanojunction," ACS Appl. Nano Mater. **5**, 5187–5195 (2022).
[25]M. Brütting, J. M. Foerster, and S. Kümmel, "Understanding primary charge separation in the heliobacterial reaction center," J. Phys. Chem. Lett. **14**, 3092–3102 (2023).
[26]A. Anda, L. De Vico, and T. Hansen, "Intermolecular modes between LH2 bacteriochlorophylls and protein residues: The effect on the excitation energies," J. Phys. Chem. B **121**, 5499–5508 (2017).
[27]G. McDermott, S. M. Prince, A. A. Freer, A. M. Hawthornthwaite-Lawless, M. Z. Papiz, R. J. Cogdell, and N. W. Isaacs, "Crystal structure of an integral membrane light-harvesting complex from photosynthetic bacteria," Nature **374**, 517–521 (1995).

07 May 2026 10:57:55

© Author(s) 2025

[28]A. Freer, S. Prince, K. Sauer, M. Papiz, A. H. Lawless, G. McDermott, R. Cogdell, and N. W. Isaacs, "Pigment–pigment interactions and energy transfer in the antenna complex of the photosynthetic bacterium *Rhodopseudomonas acidophila*," Structure **4**, 449–462 (1996).
[29]V. Sundström, T. Pullerits, and R. Van Grondelle, "Photosynthetic light-harvesting: Reconciling dynamics and structure of purple bacterial LH2 reveals function of photosynthetic unit," J. Phys. Chem. B **103**, 2327–2346 (1999).
[30]X. Hu, T. Ritz, A. Damjanović, F. Autenrieth, and K. Schulten, "Photosynthetic apparatus of purple bacteria," Q. Rev. Biophys. **35**, 1–62 (2002).
[31]R. van Grondelle and V. I. Novoderezhkin, "Energy transfer in photosynthesis: Experimental insights and quantitative models," Phys. Chem. Chem. Phys. **8**, 793–807 (2006).
[32]Y. Saga, Y. Shibata, and H. Tamiaki, "Spectral properties of single light-harvesting complexes in bacterial photosynthesis," J. Photochem. Photobiol., C **11**, 15–24 (2010).
[33]E. Keil, H. Lokstein, R. Cogdell, J. Hauer, D. Zigmantas, and E. Thyrhaug, "Light harvesting in purple bacteria does not rely on resonance fine-tuning in peripheral antenna complexes," Photosynth. Res. **161**, 191–201 (2024).
[34]J. R. Reimers, M. Biczysko, D. Bruce, D. F. Coker, T. J. Frankcombe, H. Hashimoto, J. Hauer, R. Jankowiak, T. Kramer, J. Linnanto, F. Mamedov, F. Müh, M. Rätsep, T. Renger, S. Styring, J. Wan, Z. Wang, Z.-Y. Wang-Otomo, Y.-X. Weng, C. Yang, J.-P. Zhang, A. Freiberg, and E. Krausz, "Challenges facing an understanding of the nature of low-energy excited states in photosynthesis," Biochim. Biophys. Acta, Bioenerg. **1857**, 1627–1640 (2016).
[35]T. Mirkovic, E. E. Ostroumov, J. M. Anna, R. van Grondelle, Govindjee, and G. D. Scholes, "Light absorption and energy transfer in the antenna complexes of photosynthetic organisms," Chem. Rev. **117**, 249–293 (2017).
[36]G. S. Engel, T. R. Calhoun, E. L. Read, T.-K. Ahn, T. Mančal, Y.-C. Cheng, R. E. Blankenship, and G. R. Fleming, "Evidence for wavelike energy transfer through quantum coherence in photosynthetic systems," Nature **446**, 782–786 (2007).
[37]G. D. Scholes, "Quantum-coherent electronic energy transfer: Did nature think of it first?," J. Phys. Chem. Lett. **1**, 2–8 (2010); arXiv:1206.5812v1.
[38]J. Strümpfer, M. Şener, and K. Schulten, "How quantum coherence assists photosynthetic light-harvesting," J. Phys. Chem. Lett. **3**, 536–542 (2012).
[39]J. Yuen-Zhou, J. J. Krich, and A. Aspuru-Guzik, "A witness for coherent electronic vs vibronic-only oscillations in ultrafast spectroscopy," J. Chem. Phys. **136**, 234501 (2012).
[40]M. B. Plenio, J. Almeida, and S. F. Huelga, "Origin of long-lived oscillations in 2D-spectra of a quantum vibronic model: Electronic versus vibrational coherence," J. Chem. Phys. **139**, 235102 (2013).
[41]F. Fassioli, R. Dinshaw, P. C. Arpin, and G. D. Scholes, "Photosynthetic light harvesting: Excitons and coherence," J. R. Soc. Interface **11**, 20130901 (2014).
[42]A. Chenu and G. D. Scholes, "Coherence in energy transfer and photosynthesis," Annu. Rev. Phys. Chem. **66**, 69–96 (2015).
[43]H. G. Duan, V. I. Prokhorenko, R. J. Cogdell, K. Ashraf, A. L. Stevens, M. Thorwart, and R. J. D. Miller, "Nature does not rely on long-lived electronic quantum coherence for photosynthetic energy transfer," Proc. Natl. Acad. Sci. U. S. A. **114**, 8493–8498 (2017).
[44]F. Caycedo-Soler, J. Lim, S. Oviedo-Casado, N. F. van Hulst, S. F. Huelga, and M. B. Plenio, "Theory of excitonic delocalization for robust vibronic dynamics in LH2," J. Phys. Chem. Lett. **9**, 3446–3453 (2018); arXiv:1804.04679.
[45]J. Cao, R. J. Cogdell, D. F. Coker, H.-G. Duan, J. Hauer, U. Kleinekathöfer, T. L. C. Jansen, T. Mančal, R. J. D. Miller, J. P. Ogilvie, V. I. Prokhorenko, T. Renger, H.-S. Tan, R. Tempelaar, M. Thorwart, E. Thyrhaug, S. Westenhoff, and D. Zigmantas, "Quantum biology revisited," Sci. Adv. **6**, eaaz4888 (2020).
[46]T. Mančal, "A decade with quantum coherence: How our past became classical and the future turned quantum," Chem. Phys. **532**, 110663 (2020).
[47]S. Kundu and N. Makri, "Real-time path integral simulation of exciton-vibration dynamics in light-harvesting bacteriochlorophyll aggregates," J. Phys. Chem. Lett. **11**, 8783–8789 (2020).
[48]R. G. Alden, E. Johnson, V. Nagarajan, W. W. Parson, C. J. Law, and R. G. Cogdell, "Calculations of spectroscopic properties of the LH2 bacteriochlorophyll–protein antenna complex from *Rhodopseudomonas acidophila*," J. Phys. Chem. B **101**, 4667–4680 (1997).
[49]J. Linnanto, J. E. I. Korppi-Tommola, and V. M. Helenius, "Electronic states, absorption spectrum and circular dichroism spectrum of the photosynthetic bacterial LH2 antenna of *Rhodopseudomonas acidophila* as predicted by exciton theory and semiempirical calculations," J. Phys. Chem. B **103**, 8739–8750 (1999).
[50]S. Tretiak, C. Middleton, V. Chernyak, and S. Mukamel, "Exciton Hamiltonian for the bacteriochlorophyll system in the LH2 antenna complex of purple bacteria," J. Phys. Chem. B **104**, 4519–4528 (2000).
[51]J. Neugebauer, "Photophysical properties of natural light-harvesting complexes studied by subsystem density functional theory," J. Phys. Chem. B **112**, 2207–2217 (2008).
[52]J. M. Linnanto and J. E. I. Korppi-Tommola, "Modelling excitonic energy transfer in the photosynthetic unit of purple bacteria," Chem. Phys. **357**, 171–180 (2009).
[53]J. Strümpfer and K. Schulten, "The effect of correlated bath fluctuations on exciton transfer," J. Chem. Phys. **134**, 095102 (2011).
[54]T. Renger and F. Müh, "Understanding photosynthetic light-harvesting: A bottom up theoretical approach," Phys. Chem. Chem. Phys. **15**, 3348–3371 (2013).
[55]T. Renger, M. E.-A. Madjet, M. Schmidt am Busch, J. Adolphs, and F. Müh, "Structure-based modeling of energy transfer in photosynthesis," Photosynth. Res. **116**, 367–388 (2013).
[56]S. Jurinovich, G. Pescitelli, L. Di Bari, and B. Mennucci, "A TDDFT/MMPol/PCM model for the simulation of exciton-coupled circular dichroism spectra," Phys. Chem. Chem. Phys. **16**, 16407 (2014).
[57]C. P. van der Vegte, J. D. Prajapati, U. Kleinekathöfer, J. Knoester, and T. L. C. Jansen, "Atomistic modeling of two-dimensional electronic spectra and excited-state dynamics for a light harvesting 2 complex," J. Phys. Chem. B **119**, 1302–1313 (2015).
[58]T. Brixner, R. Hildner, J. Köhler, C. Lambert, and F. Würthner, "Exciton transport in molecular aggregates – from natural antennas to synthetic chromophore systems," Adv. Energy Mater. **7**, 1700236 (2017).
[59]M. I. Mallus, M. Schallwig, and U. Kleinekathöfer, "Relation between vibrational dephasing time and energy gap fluctuations," J. Phys. Chem. B **121**, 6471–6478 (2017).
[60]A. Sisto, C. Stross, M. W. van der Kamp, M. O'Connor, S. McIntosh-Smith, G. T. Johnson, E. G. Hohenstein, F. R. Manby, D. R. Glowacki, and T. J. Martinez, "Atomistic non-adiabatic dynamics of the LH2 complex with a GPU-accelerated *ab initio* exciton model," Phys. Chem. Chem. Phys. **19**, 14924–14936 (2017).
[61]L. Cupellini, S. Caprasecca, C. A. Guido, F. Müh, T. Renger, and B. Mennucci, "Coupling to charge transfer states is the key to modulate the optical bands for efficient light harvesting in purple bacteria," J. Phys. Chem. Lett. **9**, 6892–6899 (2018).
[62]S. Bourne Worster, C. Stross, F. M. W. C. Vaughan, N. Linden, and F. R. Manby, "Structure and efficiency in bacterial photosynthetic light harvesting," J. Phys. Chem. Lett. **10**, 7383–7390 (2019); arXiv:1908.08373.
[63]F. Cardoso Ramos, M. Nottoli, L. Cupellini, and B. Mennucci, "The molecular mechanisms of light adaption in light-harvesting complexes of purple bacteria revealed by a multiscale modeling," Chem. Sci. **10**, 9650–9662 (2019).
[64]V. Sláma, L. Cupellini, and B. Mennucci, "Exciton properties and optical spectra of light harvesting complex II from a fully atomistic description," Phys. Chem. Chem. Phys. **22**, 16783–16795 (2020).
[65]R. Y. Pishchalnikov, D. D. Chesalin, and A. P. Razjivin, "The relationship between the spatial arrangement of pigments and exciton transition moments in photosynthetic light-harvesting complexes," Int. J. Mol. Sci. **22**, 10031 (2021).
[66]T. Renger, "Semiclassical modified Redfield and generalized Förster theories of exciton relaxation/transfer in light-harvesting complexes: The quest for the principle of detailed balance," J. Phys. Chem. B **125**, 6406–6416 (2021).
[67]C. Friedl, D. G. Fedorov, and T. Renger, "Towards a quantitative description of excitonic couplings in photosynthetic pigment–protein complexes: Quantum chemistry driven multiscale approaches," Phys. Chem. Chem. Phys. **24**, 5014–5038 (2022).
[68]S. Kundu, R. Dani, and N. Makri, "B800-to-B850 relaxation of excitation energy in bacterial light harvesting: All-state, all-mode path integral simulations," J. Chem. Phys. **157**, 015101 (2022).
[69]E. Zerah Harush and Y. Dubi, "Signature of quantum coherence in the exciton energy pathways of the LH2 photosynthetic complex," ACS Omega **8**, 38871–38878 (2023).

07 May 2026 10:57:55

© Author(s) 2025

[70]V. I. Novoderezhkin, "Excitation dynamics in photosynthetic light-harvesting complex B850: Exact solution versus Redfield and Förster limits," Phys. Chem. Chem. Phys. **25**, 14219–14231 (2023).
[71]I. Schelter and S. Kümmel, "Accurate evaluation of real-time density functional theory providing access to challenging electron dynamics," J. Chem. Theory Comput. **14**, 1910–1927 (2018).
[72]K. Yabana and G. F. Bertsch, "Time-dependent local-density approximation in real time," Phys. Rev. B **54**, 4484–4487 (1996).
[73]A. Bruner, D. LaMaster, and K. Lopata, "Accelerated broadband spectra using transition dipole decomposition and Padé approximants," J. Chem. Theory Comput. **12**, 3741–3750 (2016).
[74]X. Andrade, D. Strubbe, U. De Giovannini, A. H. Larsen, M. J. T. Oliveira, J. Alberdi-Rodriguez, A. Varas, I. Theophilou, N. Helbig, M. J. Verstraete, L. Stella, F. Nogueira, A. Aspuru-Guzik, A. Castro, M. A. L. Marques, and A. Rubio, "Real-space grids and the Octopus code as tools for the development of new simulation approaches for electronic systems," Phys. Chem. Chem. Phys. **17**, 31371–31396 (2015); arXiv:1501.05654v1.
[75]J. Jornet-Somoza, J. Alberdi-Rodriguez, B. F. Milne, X. Andrade, M. A. L. Marques, F. Nogueira, M. J. T. Oliveira, J. J. P. Stewart, and A. Rubio, "Insights into colour-tuning of chlorophyll optical response in green plants," Phys. Chem. Chem. Phys. **17**, 26599–26606 (2015).
[76]J. Jornet-Somoza and I. Lebedeva, "Real-time propagation TDDFT and density analysis for exciton coupling calculations in large systems," J. Chem. Theory Comput. **15**, 3743–3754 (2019).
[77]M. Kick, E. Alexander, A. Beiersdorfer, and T. V. Voorhis, "Super-resolution techniques to simulate electronic spectra of large molecular systems," Nat. Commun. **15**, 8001 (2024).
[78]I. Schelter, J. M. Foerster, A. T. Gardiner, A. W. Roszak, R. J. Cogdell, G. M. Ullmann, T. B. de Queiroz, and S. Kümmel, "Assessing density functional theory in real-time and real-space as a tool for studying bacteriochlorophylls and the light-harvesting complex 2," J. Chem. Phys. **151**, 134114 (2019).
[79]J. Kehrer, R. Richter, J. M. Foerster, I. Schelter, and S. Kümmel, "Self-interaction correction, electrostatic, and structural influences on time-dependent density functional theory excitations of bacteriochlorophylls from the light-harvesting complex 2," J. Chem. Phys. **153**, 144114 (2020).
[80]T. Trepl, I. Schelter, and S. Kümmel, "Analyzing excitation-energy transfer based on the time-dependent density functional theory in real time," J. Chem. Theory Comput. **18**, 6577–6587 (2022).
[81]G. Van Rossum and F. L. Drake, *Python 3 Reference Manual* (CreateSpace, Scotts Valley, CA, 2009).
[82]P. Virtanen, R. Gommers, T. E. Oliphant, M. Haberland, T. Reddy, D. Cournapeau, E. Burovski, P. Peterson, W. Weckesser, J. Bright, S. J. van der Walt, M. Brett, J. Wilson, K. J. Millman, N. Mayorov, A. R. J. Nelson, E. Jones, R. Kern, E. Larson, C. J. Carey, İ. Polat, Y. Feng, E. W. Moore, J. VanderPlas, D. Laxalde, J. Perktold, R. Cimrman, I. Henriksen, E. A. Quintero, C. R. Harris, A. M. Archibald, A. H. Ribeiro, F. Pedregosa, P. van Mulbregt, and SciPy 1.0 Contributors, "SciPy 1.0: Fundamental algorithms for scientific computing in Python," Nat. Methods **17**, 261–272 (2020).
[83]P. R. Vaidyanathan, "A modified version of the *cubetools.py* Python module," https://gist.github.com/aditya95sriram/8d1fccbb91dae93c4edf31cd6a22510f (2017).
[84]I. Schelter and R. Richter, "Bayreuth spectrum evaluation script *BTevalSpec.py* v1.11," https://github.com/IngoSchelterUBT/BTevalSpec (2025).
[85]W. Humphrey, A. Dalke, and K. Schulten, "VMD: Visual molecular dynamics," J. Mol. Graphics **14**, 33–38 (1996).
[86]L. Kleinman and D. M. Bylander, "Efficacious form for model pseudopotentials," Phys. Rev. Lett. **48**, 1425–1428 (1982).
[87]N. Troullier and J. L. Martins, "Efficient pseudopotentials for plane-wave calculations," Phys. Rev. B **43**, 1993–2006 (1991).
[88]M. A. L. Marques, X. López, D. Varsano, A. Castro, and A. Rubio, "Time-dependent density-functional approach for biological chromophores: The case of the green fluorescent protein," Phys. Rev. Lett. **90**, 258101 (2003).
[89]T. Stein, L. Kronik, and R. Baer, "Reliable prediction of charge transfer excitations in molecular complexes using time-dependent density functional theory," J. Am. Chem. Soc. **131**, 2818–2820 (2009).
[90]H. Aksu, A. Schubert, E. Geva, and B. D. Dunietz, "Explaining spectral asymmetries and excitonic characters of the core pigment pairs in the bacterial reaction center using a screened range-separated hybrid functional," J. Phys. Chem. B **123**, 8970–8975 (2019).
[91]M. Brütting, J. M. Foerster, and S. Kümmel, "Investigating primary charge separation in the reaction center of *Heliobacterium modesticaldum*," J. Phys. Chem. B **125**, 3468–3475 (2021).
[92]Z. Hashemi and L. Leppert, "Assessment of the *ab initio* Bethe–Salpeter equation approach for the low-lying excitation energies of bacteriochlorophylls and chlorophylls," J. Phys. Chem. A **125**, 2163–2172 (2021); arXiv:2008.00917.
[93]S. Volpert, Z. Hashemi, J. M. Foerster, M. R. G. Marques, I. Schelter, S. Kümmel, and L. Leppert, "Delocalized electronic excitations and their role in directional charge transfer in the reaction center of *Rhodobacter sphaeroides*," J. Chem. Phys. **158**, 195102 (2023).
[94]C. Andrea Rozzi, S. Maria Falke, N. Spallanzani, A. Rubio, E. Molinari, D. Brida, M. Maiuri, G. Cerullo, H. Schramm, J. Christoffers, and C. Lienau, "Quantum coherence controls the charge separation in a prototypical artificial light-harvesting system," Nat. Commun. **4**, 1602 (2013).
[95]S. M. Falke, C. A. Rozzi, D. Brida, M. Maiuri, M. Amato, E. Sommer, A. De Sio, A. Rubio, G. Cerullo, E. Molinari, and C. Lienau, "Coherent ultrafast charge transfer in an organic photovoltaic blend," Science **344**, 1001–1005 (2014).
[96]F. Calvayrac, P.-G. Reinhard, E. Suraud, and C. A. Ullrich, "Nonlinear electron dynamics in metal clusters," Phys. Rep. **337**, 493–578 (2000).
[97]S. J. Akram, S. Meißner, and S. Kümmel, "Analyzing electronic excitations and exciton binding energies in Y6 films," Adv. Funct. Mater. (published online 2025).
[98]M. Dahlbom, T. Pullerits, S. Mukamel, and V. Sundström, "Exciton delocalization in the B850 light-harvesting complex: Comparison of different measures," J. Phys. Chem. B **105**, 5515–5524 (2001).
[99]A. T. Gardiner, A. W. Roszak, and R. J. Cogdell, "Crystal structure of the LH2 complex from rhodoblastus acidophilus (strain 10050) at 1.85Å resolution," private communication (2015), cf. Ref. 78.
[100]M. Z. Papiz, S. M. Prince, T. Howard, R. J. Cogdell, and N. W. Isaacs, "The structure and thermal motion of the B800–850 LH2 complex from *Rps.acidophila* at 2.0Å resolution and 100K: New structural features and functionally relevant motions," J. Mol. Biol. **326**, 1523–1538 (2003).
[101]G. Henkelman, A. Arnaldsson, and H. Jónsson, "A fast and robust algorithm for Bader decomposition of charge density," Comput. Mater. Sci. **36**, 354–360 (2006).
[102]D. Hofmann, T. Körzdörfer, and S. Kümmel, "Energy transfer and Förster's dipole coupling approximation investigated in a real-time Kohn-Sham scheme," Phys. Rev. A **82**, 012509 (2010).
[103]A. Anda, T. Hansen, and L. De Vico, "Multireference excitation energies for bacteriochlorophylls a within light harvesting system 2," J. Chem. Theory Comput. **12**, 1305–1313 (2016).
[104]A. Anda, T. Hansen, and L. De Vico, "Q_y and Q_x absorption bands for bacteriochlorophyll a molecules from LH2 and LH3," J. Phys. Chem. A **123**, 5283–5292 (2019).
[105]D. Hofmann-Mees, H. Appel, M. Di Ventra, and S. Kümmel, "Determining excitation-energy transfer times and mechanisms from stochastic time-dependent density functional theory," J. Phys. Chem. B **117**, 14408–14419 (2013).

07 May 2026 10:57:55

© Author(s) 2025